Dalton Transactions

ROYAL SOCIETY OF CHEMISTRY

PAPER

View Article Online
View Journal | View Issue

Cite this: *Dalton Trans.*, 2020, **49**, 5302

Spin crossover in 2D iron(II) phthalazine cyanometallic complexes†

Volodymyr M. Hiiuk,[a,b,c] Sergiu Shova,[d] Aurelian Rotaru,[e] Alexander A. Golub,[c] Igor O. Fritsky[a,b] and Il'ya A. Gural'skiy *[a,b]

Received 2nd March 2020,
Accepted 24th March 2020

DOI: 10.1039/d0dt00783h

rsc.li/dalton

Two new 2D spin-crossover (SCO) analogues of Hofmann clathrates of composition $[Fe(phth)_2M^{II}(CN)_4]$ (where phth = phthalazine; M^{II} = Pd, Pt) have been synthesized and their structures and switchable behaviour have been characterized. Single-crystal X-ray analysis reveals that the Pt and Pd derivatives contain Fe^{II} centres equatorially surrounded by four equivalent μ_4-$[M^{II}(CN)_4]^{2-}$ groups. Two crystallographically equivalent phthalazine (phth) ligands occupy the axial positions of each Fe^{II} site, completing its octahedral coordination environment. The stabilization of these structures is realized *via* supramolecular C–H···M interactions and π–π stacking. Temperature-dependent magnetic susceptibility measurements showed that Pt ($T_{1/2}\downarrow$ = 211 K and $T_{1/2}\uparrow$ = 218 K) and Pd ($T_{1/2}\downarrow$ = 202 K and $T_{1/2}\uparrow$ = 207 K) derivatives display cooperative spin crossover with narrow thermal hysteresis loops. In addition, spin crossover in these complexes was characterized by optical measurements, differential scanning calorimetry, and IR and Raman spectroscopy. This research shows that the use of phthalazine leads to the production of new SCO systems with attractive transition characteristics and opens up new perspectives for the design of switchable complexes based on fused bicyclic azine ligands.

Introduction

The study of the spin crossover (SCO) phenomenon in the coordination compounds of 3d elements attracts considerable attention from a wide community of scientists working in the fields of switchable materials, molecular machines, thermochromic elements, sensors, protective elements, *etc*.[1] High interest in this phenomenon is associated with the existence of two spin states and the possibility of a reversible switch from one state (low spin (LS)) to another (high spin (HS)) under the influence of external factors such as temperature, pressure, magnetic field, light irradiation and guest molecules.[2–5] The change in the electronic structure during spin crossover causes a sharp change in numerous physical properties of complexes. These effects make spin-crossover materials interesting for numerous practical applications.[6–9]

Hofmann clathrate-like complexes form one of the most interesting families of SCO compounds.[4] These compounds may undergo SCO above,[10–12] below[13–15] or around room temperature.[16,17] Chemically they are iron-containing polymeric frameworks supported by bridging polycyanometallate anions and N-donor aromatic ligands. De facto, a variety of these complexes are related to a number of different cyanometallates (Ni^{II}, Pd^{II}, Pt^{II}, Cu^{I}, Ag^{I}, Au^{I} and some others)[4] and a number of potential N-donor aromatic ligands (pyrimidines,[18–23] pyridines,[24–41] pyrazines,[10,11,13,14,16] and naphthyridines[17,42]) suitable for the design of these frameworks. Different combinations of organic ligands and cyanometallic co-ligands lead to SCO polymers with diverse topologies of frameworks and having different SCO properties.[14,17,43–45] In case bridging ligands are used, it is possible to obtain three-dimensional metal–organic frameworks (MOFs), which, depending on the pore size, can incorporate guest molecules of various sizes.[46–48] A nice example of such a ligand is pyrazine (pz).[16] It is worth noting that one of the representatives of the dehydrated form of the complex based on pz composition $[Fe(pz)Pt(CN)_4]$ displays hysteretic spin crossover behaviour near room temperature, which makes it convenient for practical applications.[49] In addition, the functionalization of already studied SCO unsubstituted ligands (X-py, py = pyridine, X = 3-Cl, 3-methyl, 4-methyl, 3,4-dimethyl,

[a]*Department of Chemistry, Taras Shevchenko National University of Kyiv, 64 Volodymyrska St., 01601 Kyiv, Ukraine. E-mail: illia.guralskyi@univ.kiev.ua*
[b]*UkrOrgSyntez Ltd., 67 Chervonotkatska St., 02094 Kyiv, Ukraine*
[c]*Faculty of Natural Sciences, National University of Kyiv-Mohyla Academy, 2 Skovorody St., 04070 Kyiv, Ukraine*
[d]*"Petru Poni" Institute of Macromolecular Chemistry, 41A Aleea Gr. Ghica Voda, 700487 Iasi, Romania*
[e]*Faculty of Electrical Engineering and Computer Science & Research Center MANSiD, Stefan cel Mare University, 13 Universitatii St., 720229 Suceava, Romania*

†Electronic supplementary information (ESI) available: PXRD, IR, crystal data and refinement details. CCDC: 1987603–1987606 For ESI and crystallographic data in CIF or other electronic format see DOI: 10.1039/D0DT00783H

3-NH_2;[30,50] X-pz, pz = pyrazine, X = 2-Cl, 2-Me, 2-I, 2-F[13,14]) also leads to the formation of the SCO analogues of the Hofmann clathrates with different transition characteristics. Due to this the design and production of these systems is an essential step to analyze the guest effect on SCO and its application for the detection of small molecules.

The fact that the six-membered ring diazine ligands show excellent results for production of SCO materials prompts the use of fused bicyclic compounds containing several azine donor centers.[17,42] Furthermore, implementation of bicyclic ligands (*e.g.* naphthyridines) can lead to some attractive switches. In this regard we use here a bicyclic ligand – phthalazine (phth).

Phthalazine is a diazanaphthalene with two adjacent nitrogen atoms and is a structural isomer of 1,6-naphthyridine and 2,6-naphthyridine. In addition, phthalazine is a pyridazine derivative for which SCO properties are well known.[51] Recently we have reported cooperative SCO in a series of [Fe(pdz)$_2$M^{II}(CN)$_4$] (pdz = pyridazine, M = Ni, Pd, Pt) complexes, which are sensitive to water inclusion and in turn can be interesting for guest effect studies.[51] Therefore, it was interesting to study how the additional benzene ring will affect the characteristics of spin crossover in a similar system.

Here we report the synthesis and characterization of two new cyanoheterometallic coordination complexes with a N-donor aromatic ligand phthalazine (phth) of composition [Fe(phth)$_2$M^{II}(CN)$_4$] (where M^{II} = Pd (**1**), Pt (**2**)), which are iron(II)-based two-dimensional SCO polymers.

Results and discussion

Crystallography

In order to establish the crystal structures of the obtained compounds, we carried out single crystal X-ray diffraction analysis of **1** and **2**. Their crystal structures were determined for both LS and HS states at 200 K and 260 K, respectively. It was found that both complexes crystallize in the triclinic space group $P\bar{1}$ with one formula unit per cell. In these complexes iron(II) has a coordination environment of an elongated [FeN$_6$] pseudo-octahedron. Each iron(II) centre binds to four cyanide groups in the *ab* plane and two axially coordinated phth ligands (Fig. 1a). Cyanometallic groups bridge the iron(II) ions in two directions leading to the formation of 2D layers that are (4,4)-nets of {FeM^{II}(CN)$_4$}. Such structural features are characteristic of Hofmann clathrate-like complexes.[4] The crystallographic data are summarized in Table 1. IR-spectroscopy (Fig. S1†) and PXRD diffraction (Fig. S2–S4†) of compounds **1** and **2** revealed that obtained crystals and powders are isostructural. The distances between the Fe^{II} cation and [M(CN)$_4$]$^{2-}$ are shorter than those between Fe^{II} and phthalazine ligands. There are also two crystallographically different cyanide fragments (N1≡C1–M1 and N2≡C2–M1) with just slightly different structural parameters, which in turn lead to two crystallographically different bridging chains (Fe1–N1C1–M1–C1N1–Fe1 and Fe1–N2C2–M1–C2N2–Fe1) that connect the Fe1 sites (see Table 2). A small deviation of Fe–N≡C angles from 180° provides a stronger σ-bond and, therefore, a higher ligand field.[50]

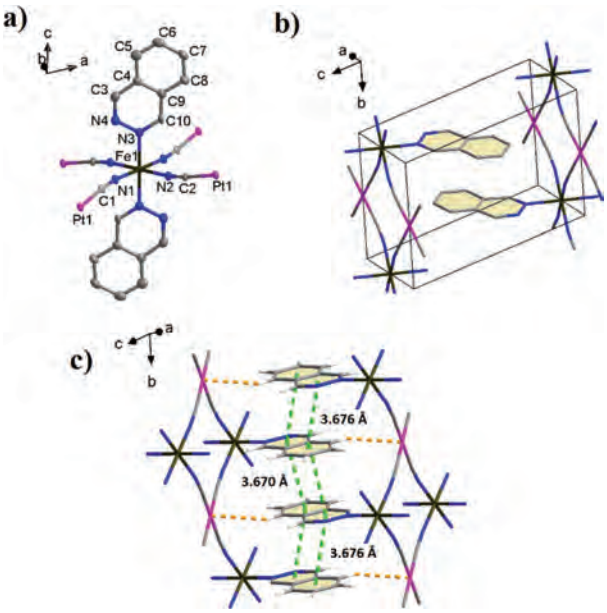

Fig. 1 Crystal structure of **2** (LS): (a) Representation of a key fragment of complex **2** (thermal ellipsoids are given at 50% probability); (b) representation of the elementary cell. Hydrogen atoms are omitted for clarity; (c) supramolecular packing *via* C–H···M interactions (orange) and π···π stacking (green). In figures a–c H atoms are omitted for clarity. [Fe: olive green, Pd: pink, N: blue, C: gray].

At 260 K the average bond distances ⟨Fe–N⟩ for **1** and **2** are equal to 2.171(4) Å and 2.167(8) Å, respectively, which correspond to the HS state of both complexes. Temperature decrease leads to the shortening of Fe–N bonds to 1.956(5) Å (for **1**) and 1.959(6) Å (for **2**), which is associated with the HS → LS transition. Consequently, after the SCO is completed, the average bond distances ⟨Fe–N⟩ are shorter by 0.215 and 0.208 Å compared to HS forms. The volume of the FeN$_6$ octahedron drops from 13.629 to 9.962 Å^3 for **1** and from 13.535 to 10.026 Å^3 for **2** upon SCO. These changes are transmitted to the lattice and the volumes of unit cells change by 6.1% (**1**) and 5.8% (**2**). Such transformations are typical, and the relative volume change is usually 5–6% for SCO complexes with FeN$_6$ coordination polyhedra.[52] However, for pyridazine derivatives, the lattice volume changes were found to be from 10% to 13%, which can be explained by the small size of the organic ligand.[51,53] The distortion parameter ($\sum|90° - \theta_{N-Fe-N}|$) shows that the geometry around the coordination centre is more distorted in the HS state with $\sum$ = 16.64° (for **1**) and $\sum$ = 18.40° (for **2**). These values decrease in the LS state down to 15.78° and 14.80° for **1** and **2** respectively. Selected bond lengths and some structural parameters are shown in Table 2.

In addition, the compounds are characterized by dense packing that is ensured by different supramolecular interactions (Fig. 1c). Selected contacts are given in Table 3.

The most striking structural features of complexes are the presence of intermolecular C5–H5···M interactions between M

Table 1 Crystallographic parameters for **1** and **2**

	$[Fe(phth)_2Pd(CN)_4]$ (**1**)		$[Fe(phth)_2Pt(CN)_4]$ (**2**)	
Temperature	200 K	260 K	200 K	260 K
Empirical formula	$C_{20}H_{12}N_8FePd$	$C_{20}H_{12}N_8FePd$	$C_{20}H_{12}N_8FePt$	$C_{20}H_{12}N_8FePt$
M_r	526.63	526.63	615.32	615.32
cryst syst	Triclinic	Triclinic	Triclinic	Triclinic
Space group	$P\bar{1}$	$P\bar{1}$	$P\bar{1}$	$P\bar{1}$
a (Å)	7.0962(7)	7.2433(4)	7.1262(5)	7.2754(8)
b (Å)	7.1676(7)	7.4455(4)	7.1724(5)	7.4315(9)
c (Å)	10.1546(16)	10.4263(9)	10.1727(8)	10.3903(14)
α (°)	71.083(11)	71.858(6)	71.020(7)	72.230(11)
β (°)	74.381(11)	69.586(6)	75.175(6)	70.501(11)
γ (°)	89.881(8)	89.943(5)	89.950(6)	89.988(10)
V (Å^3)	468.49(10)	497.11(6)	473.38(6)	501.04(11)
Z	1	1	1	1
ρ_{calc} (g cm^{-3})	1.867	1.759	2.158	2.039
μ (mm^{-1})	1.760	1.658	8.172	7.721
F(000)	260.0	260.0	292.0	292.0
Goodness-of-fit on F^2	1.022	1.141	1.052	1.048
Final R indexes [$I > = 2\sigma(I)$]	$R_1 = 0.0558$, w$R_2 = 0.1287$	$R_1 = 0.0417$, w$R_2 = 0.1113$	$R_1 = 0.0366$, w$R_2 = 0.0765$	$R_1 = 0.0546$, w$R_2 = 0.1052$
Final R indexes [all data]	$R_1 = 0.0699$, w$R_2 = 0.1362$	$R_1 = 0.0444$, w$R_2 = 0.1134$	$R_1 = 0.0371$, w$R_2 = 0.0771$	$R_1 = 0.0557$, w$R_2 = 0.1071$

$R_1 = \sum||F_o| - |F_c||/\sum|F_o|$ and $wR_2 = [\sum w(F_o^2 - F_c^2)^2/\sum w(F_o^2)^2]^{1/2}$ for $F_o^2 > 2\sigma(F_o^2)$.

Table 2 Selected bond angles and bond lengths for **1** and **2**

	$[Fe(phth)_2Pd(CN)_4]$ (**1**)		$[Fe(phth)_2Pt(CN)_4]$ (**2**)	
Temperature	200 K	260 K	200 K	260 K
Fe^{II} spin state	LS	HS	LS	HS
⟨Fe1–N1⟩ (Å)	1.937(4)	2.164(3)	1.947(6)	2.144(6)
⟨Fe1–N2⟩ (Å)	1.944(5)	2.140(3)	1.944(6)	2.144(7)
⟨Fe1–N3⟩ (Å)	1.987(5)	2.209(4)	1.987(6)	2.212(8)
$\langle Fe–N\rangle_{average}$ (Å)	1.956(5)	2.171(4)	1.959(6)	2.167(8)
$V_{oct}(FeN_6)$ (Å^3)	9.962	13.629	10.026	13.535
$\sum$ (°)	15.78	16.64	14.80	18.40
Fe1–N1C1–M1–C1N1–Fe1 (Å)	10.156(7)	10.580(5)	10.166(9)	10.566(10)
Fe1–N2C2–M1–C2N2–Fe1 (Å)	10.132(7)	10.528(5)	10.156(9)	10.532(10)
∠Fe1–N1–C1 (°)	171.8(5)	160.7(3)	171.4(6)	161.1(7)
∠Fe1–N2–C2 (°)	171.1(5)	163.8(3)	172.3(6)	164.3(8)

Table 3 Selected intermolecular contacts for **1** and **2**

	$[Fe(phth)_2Pd(CN)_4]$ (**1**)		$[Fe(phth)_2Pt(CN)_4]$ (**2**)	
Temperature	200 K	260 K	200 K	260 K
Spin state	LS	HS	LS	HS
C–H···M interactions				
C5–H5···M (Å)	2.8816(5)	2.7632(3)	2.9432(3)	2.8479(6)
C5···M (Å)	3.724(6)	3.616(5)	3.790(7)	3.713(10)
∠C5–H5···M (°)	151.3(4)	152.9(4)	152.1(5)	155.3(7)
π–π stacking				
C_{ring}–C'_{ring}	3.6734(4)	3.8135(2)	3.6760(2)	3.8073(5)
	3.6643(4)	3.7898(2)	3.6704(3)	3.7970(4)
∠N3–C_{ring}–C'_{ring} (°)	102.2(2)	101.2(2)	101.6(3)	102.2(3)
	101.3(2)	98.3(2)	101.6(3)	97.2(3)
∠C5–C_{ring}–C'_{ring} (°)	89.4(3)	89.8(3)	88.8(4)	87.1(5)
	71.9(3)	69.1(3)	71.4(4)	70.2(5)

where C_{ring} is the centroid of the phthalazine ring.

(where M = Pd, Pt) and two H5 atoms of the independent phth ligands due to the crystal packing effect. The nature of these interactions has been studied and clearly described in other papers.[54,55] As an example, analogous intermolecular C–H···M interactions (where M = Pd, Pt) have been reported for a homoleptic xanthate and dithiocarbamates.[56,57] The organometallic complexes with this type of interaction attract attention because of their possible involvement in C–H bond activation.[56,58]

At 260 K the C5–H5···M distances for **1** and **2** are equal to 2.7632(3) Å and 2.8479(6) Å. Temperature decrease leads to the elongation of C5–H5···M contacts by 0.118 and 0.095 Å. The values of C5···M distances change by 3.0% (**1**) and 2.1% (**2**). On the other hand, the C5–H5···M angle variations are also observed upon spin crossover: from 152.9(4)° (260 K) to 151.3 (4)° (200 K) for C5–H5···Pd and from 155.3(7)° (260 K) to 152.1 (5)° (200 K) for C5–H5···Pt.

In addition, phthalazine ligands are oriented in such a way as to ensure pseudooctahedral coordination with the M (where M = Pd, Pt) center. The value of the H5···M···H5′ angle of 180° indicates that the intermolecular interactions are collinear. The selected parameters indicating the occurrence of these weak contacts are given in Table 3.

The protruding phthalazine ligands of adjacent layers are packed in an offset face to face fashion forming π–π displaced stacking interactions (Fig. 1c). There are two sets of short π-stacking observed. These two sets of π-overlaps between the phth ligands of the adjacent {Fe(phth)$_2$} chains take turns alternating along the *b* axis. The weak π–π contacts additionally stabilize the structures, with centroid–centroid distances of 3.66–3.68 Å in the LS state and 3.78–3.81 Å in the HS state. These values are slightly larger than those found for pyridazine complexes.[51] This may be explained by the fact that phthalazine is a more sterically large ligand than pyridazine.

The presence of weak π–π stacking interactions between the aromatic rings and intermolecular C–H···M interactions plays an important role in the architecture of the complexes. Due to such interactions the adjacent chains are held together giving rigidity to the structure. Moreover, this may explain a moderate degree of cooperativity in these compounds and no voids are available in the structure.

Magnetic properties

The most convenient method for monitoring SCO is the measurement of magnetic susceptibility (χ_M) as a function of temperature. The change in the electronic configuration of the 3d-metal ion during the spin crossover has as a consequence a sharp change in χ_M. Temperature dependence of the magnetic susceptibility recorded for powders **1** and **2** upon cooling/heating (in the range 12–300 K) is given in Fig. 2.

Complex **1** undergoes cooperative SCO with a narrow thermal hysteresis of 5 K. At room temperature, the $\chi_M T$ value is 3.55 cm^3 K mol^{-1} which is a typical value for the Fe^{II} ion in the paramagnetic HS state (S = 2). The value of $\chi_M T$ remains almost constant upon cooling until 230 K. Upon further cooling, $\chi_M T$ decreases abruptly, with $T_{1/2}\downarrow$ = 202 K attaining a value of 0.40 cm^3 K mol^{-1} at 12 K indicating that the LS state (S = 0) is practically fully populated. The subsequent heating mode provides evidence for a 5 K hysteresis loop with $T_{1/2}\uparrow$ = 207 K.

Complex **2** shows temperature dependent magnetic susceptibility similar to **1**. The $\chi_M T$ value was found to be 3.44 cm^3 K mol^{-1} at 300 K, which corresponds to the high-spin state of the iron(II) ion. Upon further cooling, $\chi_M T$ decreases abruptly attaining a value of 0.21 cm^3 K mol^{-1} at 12 K. The subsequent heating mode provides evidence for a 7 K wide hysteresis loop, characterized by the following switching temperatures: 211 K and $T_{1/2}\uparrow$ = 218 K.

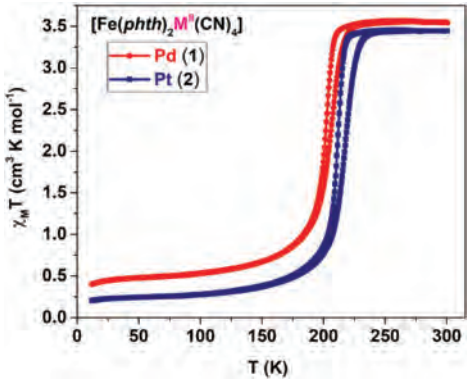

Fig. 2 Magnetic properties of **1** and **2** ($\chi_M T$ *vs.* T) determined in heating and cooling modes at a scan rate of 2 K min^{-1} under a magnetic field of 0.1 T. Graphs show that Pd (**1**) ($T_{1/2}\downarrow$ = 202 K and $T_{1/2}\uparrow$ = 207 K) and Pt (**2**) ($T_{1/2}\downarrow$ = 211 K and $T_{1/2}\uparrow$ = 218 K) complexes display cooperative spin crossover with narrow thermal hystereses.

In terms of the magnetic properties, complexes **1** and **2** undergo a complete hysteretic thermal SCO. The complete transition between the two spin states has been confirmed by temperature-dependent Raman spectroscopy (see the Spectroscopic characterization section).

Comparison of the obtained compounds with unsubstituted azines and bicyclic ligands allows us to find some similarities (Table S1†). Although phthalazine is structurally more similar to pyridazine,[51] the spin-crossover properties of phth complexes with Pt and Pd are more similar to py[16,24] derivatives having a narrow thermal hysteresis (5–8 K) at low temperatures (in the range of 208–216 K). In turn, pz[16] and pdz[51] complexes are highly cooperative systems with large hysteresis, exhibiting SCO behaviour at higher temperatures. This is due to the presence of short interlayer contacts and π–π stacking. Moreover, such a difference in the hysteresis width for pz complexes can be explained by the binding of the layers to the rigid 3D framework. Considering complexes with bicyclic systems (*e.g.* naphthyridines,[17,42] isoquinoline[59]), which are formed using dicyanoargentate anions, there are no clear trends. Isomerization of the ligands leads to different topologies of frameworks, which, in turn, lead to different SCO behaviours (two-step low temperature non-hysteretic[59] and hysteretic[42] and room temperature hysteretic[17]).

So, being the closest analogues of pdz complexes, phth derivatives demonstrate spin crossover at temperatures much lower than those found for the corresponding dehydrated forms of pyridazine derivatives ([Fe(pdz)$_2$Pd(CN)$_4$]: $T_{1/2}\downarrow$ = 247 K, $T_{1/2}\uparrow$ = 260 K; [Fe(pdz)$_2$Pt(CN)$_4$]: $T_{1/2}\downarrow$ = 269 K, $T_{1/2}\uparrow$ = 283 K).[51] As shown in Table S1,† the widest hysteresis loops were observed for hydrated forms of pyridazine-based complexes, however, the SCO in that case is not complete. For dehydrated forms, the hysteresis width was 13 and 14 K for Pd and Pt, respectively.[51] Here the hysteresis width reaches only 5

and 7 K for **1** and **2**, respectively. Such differences in the hysteresis width for pyridazine and phthalazine complexes can be due to the additional sterically bulky benzene ring, which leads to a larger separation between cyanometallic layers and weakened cooperativity.[60] However, as mentioned above, for the 2D Hofmann type spin crossover materials there are examples with both large[13,22,50] and narrow[18,22,24] thermal hysteresis.

It is worth noting that both obtained complexes display an asymmetrical shape of their hysteresis loop: the cooling branch shows a more abrupt incline than the heating branch. The same effect is well known for other SCO complexes, *e.g.* Hofmann-type coordination polymers of composition $[Fe(3\text{-}NH_2py)_2M(CN)_4]$ (3-NH_2py = 3-aminopyridine, M = Ni, Pd, Pt) display a similar curve shape.[50] This type of hysteresis loop was also observed for both hydrated forms of the $[Fe(pdz)_2M(CN)_4]\cdot H_2O$ (M = Pd, Pt) complexes and for the dehydrated form of the Pt derivative.[51]

Calorimetric measurements

Spin crossover is considered as a first-order phase transition associated with a change in the entropy of the system. Therefore, calorimetry is a powerful and effective method for detecting and studying phase transitions in iron(II)-based SCO compounds. In this case, the thermodynamic parameters upon spin crossover have characteristic values and are associated with changes in the molecular vibrations and spin multiplicity changes. Accordingly, the characteristic values of enthalpies and entropies in SCO systems correspond to the range of 10–20 kJ mol^{-1} and 50–80 J mol^{-1} K^{-1} for enthalpy and entropy, respectively.[61] The heat capacity temperature profiles for compounds **1** and **2** are shown in Fig. 3.

Graphs display exothermic peaks upon cooling at $T_{1/2}\downarrow$ = 195 K (for **1**) and 202 K (for **2**) and endothermic peaks upon heating at $T_{1/2}\uparrow$ = 204 K (for **1**) and 214 K (for **2**). The phase transition temperatures are reasonably consistent with the spin crossover temperatures found in magnetic measurements.

The small differences between DSC and magnetic data in temperature values are caused by the different sample thermalisation and the different temperature change rates used in the experiments. The calculated ΔH and ΔS values are in the range ΔH = 9–15 kJ mol^{-1} and ΔS = 47–70 J mol^{-1} K^{-1} (see Table 4) and are consistent with the typical values characteristic of Hofmann-like clathrates of Fe^{II} with SCO behaviour.[4]

Different broadness and heights of the DSC peaks for both **1** and **2** in the heating and cooling modes are explained by the type of spin crossover (gradual or abrupt) and are consistent with the magnetic data. In the cooling mode the spin crossover is more abrupt, which corresponds to a narrower and higher peak in the DSC curve. At the same time, the transitions in the heating mode for **1** and **2** are more gradual, leading to wider peaks. These features were reproducible over various temperature cycles.

Optical properties

The thermally induced SCO is always accompanied by a change in the colour due to the d–d electronic transitions between the energy levels of transition metals. Therefore, the presence of the thermochromic effect is an excellent marker for monitoring the spin crossover, which allows us to observe SCO by a change in the intensity of the reflected light. The optical reflectance for complexes **1** and **2** was followed as a function of temperature (Fig. 4a). A green filter (λ = 532 nm) was used for measurements because in this spectral region a maximum contrast between the LS and HS states can be achieved.

The typical curves confirmed the presence of a spin crossover for **1** and **2**. The values of equilibrium temperatures ($T_{1/2}\downarrow$ = 193 K and $T_{1/2}\uparrow$ = 203 K (for **1**) and $T_{1/2}\downarrow$ = 201 K and $T_{1/2}\uparrow$ = 214 K (for **2**)) are consistent with the values obtained in mag-

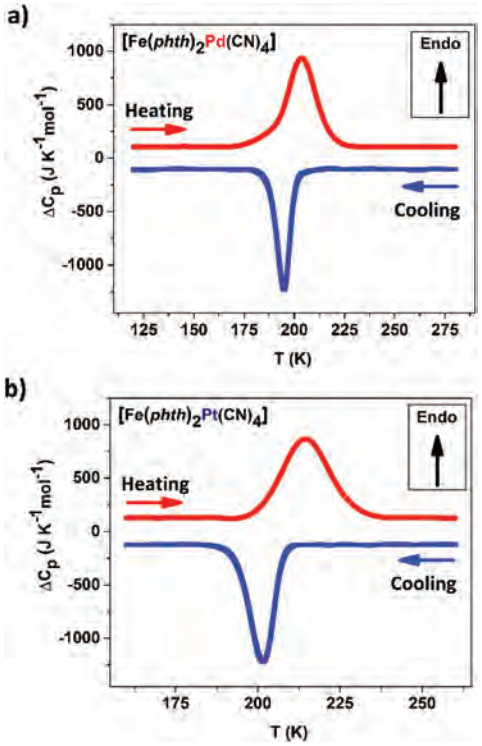

Fig. 3 DSC curves of **1** (a) and **2** (b) showing thermal effects upon SCO. Differential scanning calorimetry (DSC) measurements of **1** and **2** were carried out over the temperature range of 100–300 K in both warming and cooling modes at a scan rate of 50 K min^{-1}.

Table 4 Thermodynamic data obtained from calorimetric DSC measurements for the SCO of **1** and **2**

	$[Fe(phth)_2Pd(CN)_4]$ (**1**)	$[Fe(phth)_2Pt(CN)_4]$ (**2**)
$T_{1/2}\downarrow$ (K)	195	202
$T_{1/2}\uparrow$ (K)	204	214
ΔT (K)	9	12
$\Delta H\downarrow$ (kJ mol^{-1})	−9.2	−10.0
$\Delta H\uparrow$ (kJ mol^{-1})	14.3	15.0
$I\Delta HI^{average}$ (kJ mol^{-1})	11.7	12.5
$\Delta S\downarrow$ (J mol^{-1} K^{-1})	−47.0	−49.6
$\Delta S\uparrow$ (J mol^{-1} K^{-1})	70.0	69.9
$I\Delta SI^{average}$ (J mol^{-1} K^{-1})	58.5	59.7

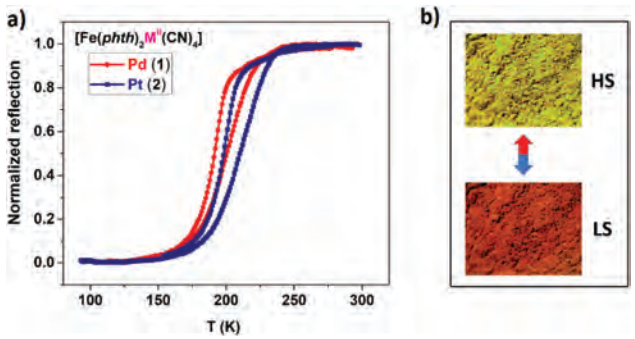

Fig. 4 (a) Normalized reflection for complexes **1** and **2** as a function of temperature. The measurements were carried out at a scan heating/cooling rate of 2 K min^{-1}. (b) Optical images of complex **2** in both spin states (LS and HS). The photograph corresponding to the HS state of **2** was recorded at room temperature. The photograph corresponding to the LS state of **2** was recorded at the temperature of liquid nitrogen.

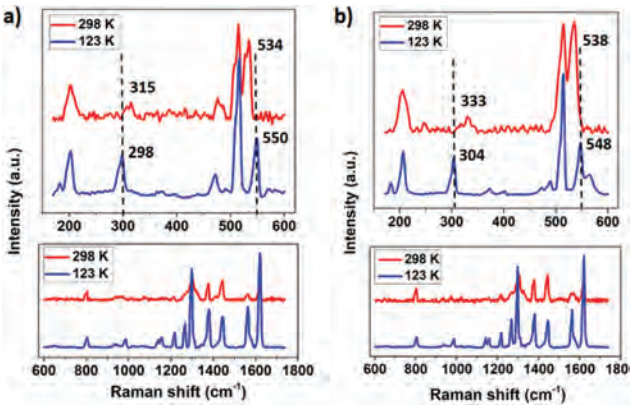

Fig. 5 Raman spectra of **1** (a) and **2** (b) powders in the low-frequency (200–600 cm^{-1}) and high-frequency (600–1600 cm^{-1}) regions at 298 K (HS) and 123 K (LS).

netic and calorimetric measurements. Minor temperature shifts compared to other measurements are associated with the different thermalisation rates of the samples. Optical images of the powder form of **2**, taken at room temperature and at 77 K (the temperature of liquid nitrogen), clearly demonstrate the thermochromic effect caused by the spin crossover (Fig. 4b). All complexes have an orange colour in the HS state and a red colour in the LS state, respectively, which make them attractive as thermochromic indicators, protective elements, *etc*.

Spectroscopic characterization

Spin crossover induces noticeable changes in the vibrational spectra in both LS and HS spin states of complexes which are associated with electronic reorganization upon spin crossover.[62,63]

Infrared spectroscopy

The FT-IR spectra of powders of **1** and **2** (Fig. S1†) were found to be very similar to those reported for the analogues of Hoffmann clathrates.[4] The strong bands associated with the C≡N stretching vibration were found at 2167 and 2165 cm^{-1} in the spectra of complexes **1** and **2**, respectively. The vibrational bands recorded at 1380–1490 cm^{-1} correspond to the C–N, C=N stretching vibrations of the phthalazine ring. The in-plane bending vibrations of C–N at 954–957 cm^{-1} were found to be shifted compared to the free phthalazine (953 cm^{-1}). The ring C–C and C–N stretching vibrations in aromatic rings appear in the region 1430–1625 cm^{-1}.

In addition, Raman spectroscopy was used (Fig. 5) since the use of this technique, in contrast to FT-IR spectroscopy, makes it possible to record the vibrational spectra in the low frequency region, wherein one can observe metal–ligand stretching vibrations as an efficient spin state marker. Moreover, technical setups allowed us to follow the temperature-dependent Raman spectra of the samples.

Raman spectroscopy

While both Mössbauer and Raman spectroscopy are powerful (complementary to magnetometry) tools to follow the completeness of SCO, each has its own advantages.

Even though Mössbauer spectroscopy allows us to directly determine the ratio of high- and low-spin Fe^{II} ions, Raman spectroscopy is a much faster method allowing more detailed (temperature) studies. Here we observed the complete disappearance of some characteristic Raman peaks and their appearance at different wavelengths which clearly indicate that the spin crossover is complete in both directions.

The stretching vibrations of the Fe–N bonds were found at 315 cm^{-1} and 333 cm^{-1} for complexes **1** and **2**, respectively. Upon lowering the temperature to 123 K, these vibrational bands are shifted to the low-frequency region by 17 cm^{-1} and 29 cm^{-1}, respectively, indicating the spin state switching to the LS state. The characteristic markers shift from 534 cm^{-1} to 550 cm^{-1} (Δ = 16 cm^{-1}) for **1** and from 538 cm^{-1} to 548 cm^{-1} (Δ = 10 cm^{-1}) for **2** which are also distinctive and correspond to the stretching vibrations of the M–C bonds, once again clearly demonstrating the spin state change in the powder forms of **1** and **2**. The complete disappearance of the peaks responsible for stretching vibrations of the M–C bonds at 534–538 cm^{-1} and their appearance at a different wavelength indicate that the spin crossover is complete in both spin states.

It should be noted that Raman spectroscopy is not a quantitative method. Therefore, the change in the spin state of the iron(II) ions was confirmed using a spin crossover curve obtained by plotting the intensity ratio of two Raman bands against temperature. The most distinctive and informative variations of the intensity ratio were observed for the 1443 and 1619 cm^{-1} modes from 1.35 at 298 K to 0.33 at 123 K for compound **1** and for the 1378 and 1619 cm^{-1} modes from 1.30 at 298 K to 0.36 at 123 K for compound **2**. The plot of the temperature dependence of the intensity ratio of these Raman modes is shown in Fig. 6 and it corresponds closely to the

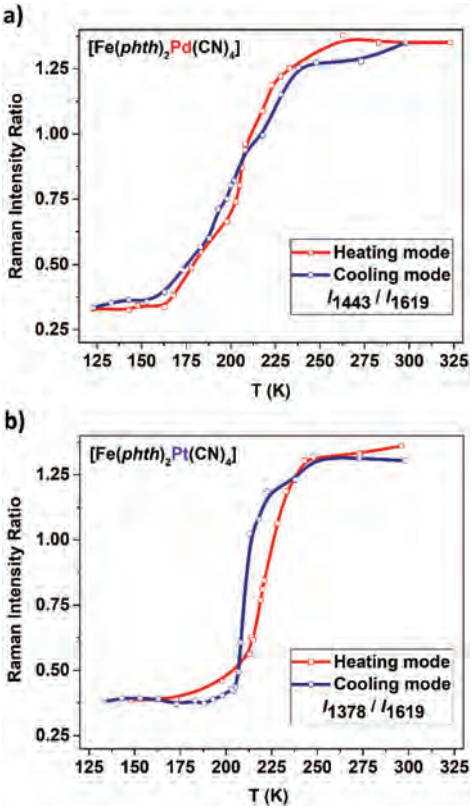

Fig. 6 Temperature dependence of the intensity ratio of two Raman modes for bulk powders **1** (a) and **2** (b) in cooling/heating modes.

curves observed in the magnetic and optical measurements. The values of equilibrium temperatures (**1**: $T_{1/2}\downarrow$ = 201 and $T_{1/2}\uparrow$ = 206; **2**: $T_{1/2}\downarrow$ = 211 and $T_{1/2}\uparrow$ = 220) are consistent with the values obtained using other techniques.

Conclusions

In summary, using phthalazine as a ligand leads to the production of new SCO systems with attractive transition characteristics. Both phthalazine cyanometallic complexes exhibit a hysteretic behaviour which makes them interesting candidates for the preparation of new switchable multifunctional materials. In addition, this work opens up new perspectives to obtain new SCO materials based on fused bicyclic azine ligands along with naphthyridines used previously.[17,42] The presence of weak π–π stacking interactions between the aromatic rings and intermolecular C–H···M interactions plays an important role in the architecture of the complexes. Due to such interactions the adjacent chains are held together giving rigidity to the structure which explains the moderate degree of cooperativity observed in these compounds. By comparing iron (II) complexes based on phthalazine and pyridazine ligands, it was shown that the inclusion of an additional benzene ring in an organic ligand leads to a decrease of the switching temperatures and a decrease of the hysteresis loop width. In addition, the spin-crossover process observed in the reported complexes is accompanied by a sharp colour change from light yellow (HS) to dark red (LS), which makes them interesting as temperature-sensitive thermochromic materials, *e.g.* thermochromic indicators, protective elements, *etc*.

Experimental

Materials and general procedures

Anhydrous potassium tetracyanometallates ($K_2[M^{II}(CN)_4]$, M^{II} = Pd, Pt), ascorbic acid ($C_6H_8O_6$) and *p*-toluenesulfonic acid monohydrate ($C_7H_8SO_3{\cdot}H_2O$) were purchased from commercial sources (Sigma Aldrich). Iron powder (Fe), phthalazine (phth, $C_8H_6N_2$) and methanol (MeOH) were provided by UkrOrgSyntez Ltd. All reagents and chemicals were of analytical- or reagent-grade purity and used as received. Iron(II) *p*-toluenesulfonate hexahydrate ($Fe(OTs)_2{\cdot}6H_2O$) was prepared by the reaction between iron powder and *p*-toluenesulfonic acid according to the procedure described previously (see ESI†).

Synthesis of 1 and 2 powder

Complexes **1** and **2** were prepared by mixing an aqueous solution (1 mL) of $K_2[M^{II}(CN)_4]$ (where M^{II} = Pd, Pt) (0.05 mmol) and phthalazine (0.10 mmol) with methanolic solutions (1 mL) containing stoichiometric amounts of $Fe(OTs)_2{\cdot}6H_2O$ (0.05 mmol) and 0.1 mg of ascorbic acid. The yellow precipitate was removed by centrifugation, washed with H_2O and MeOH successively, and dried in air. Yield = 70.5% (**1**) and 67% (**2**). Elemental analysis of $C_{20}H_{12}PdFeN_8$ (**1**) (526): calcd C, 45.61; H, 2.30; N, 21.28; found C, 45.49; H, 2.35; N, 21.14%; FT-IR (cm^{-1}): 2167(s), 1623(w), 1579(w), 1564(w), 1490(w), 1445(w), 1379(m), 1278(m), 1245(w), 1217(m), 1157(w), 1137(w), 977(w), 969(w), 955(w), 937(m), 921(s), 866(w), 824(w), 783(w), 757(s), 655(m), 516(w), 417(s), 407(m). $C_{20}H_{12}PtFeN_8$ (**2**) (615): calcd C, 39.04; H, 1.97; N, 18.21; found C, 39.48; H, 2.07; N, 18.17%; FT-IR (cm^{-1}): 2165(s), 1622(w), 1578(w), 1564(w), 1490(w), 1445(w), 1379(m), 1277(m), 1245(w), 1217(m), 1158(w), 1138(w), 977(w), 969(w), 954(w), 937(m), 919(s), 868(w), 824(w), 783(w), 757(s), 655(m), 516(w), 468(s), 455(s), 444(m).

Crystallization

Single crystals of **1** and **2** were grown *via* a slow-diffusion method within three layers in a 5 mL tube. $K_2[M^{II}(CN)_4]$ (where M^{II} = Pd, Pt) (0.05 mmol) and phthalazine (0.10 mmol) in water (1 ml) from one side and $Fe(OTs)_2{\cdot}6H_2O$ (0.05 mmol) and 0.1 mg of ascorbic acid in methanol (1 mL) from another side were let to diffuse through a layer of water–methanol (1 : 1, 2 ml) for 3 weeks. Orange crystals were obtained. Crystal were kept in the mother solution prior to the subsequent measurements.

X-ray structure determination

Single-crystal X-ray diffraction analysis of **1** and **2** was performed on an Oxford-Diffraction XCALIBUR E CCD diffract-

ometer with graphite-monochromated Mo-Kα radiation. XRD data at 260 K and 200 K for **1** and **2** were collected. The unit cell determination and data integration were carried out using the CrysAlisPro package from Oxford Diffraction. Multi-scan correction for absorption was applied. Both structures were solved using an intrinsic phasing method using SHELXT and refined by full-matrix least-squares on F^2 with SHELXL[64,65] using the graphical interface of Olex2.[66] Non-hydrogen atoms were refined anisotropically. Aromatic hydrogen atoms were geometrically fixed and refined using a riding model. Crystallographic data for **1** and **2** are listed in Tables S3–S6.† Specific details of each refinement are given in the crystallographic information files (CIF-files). Crystallographic data for the structures have been deposited with the Cambridge Crystallographic Data Centre, CCDC: 1987603 (**1**–200 K), 1987604 (**1**–260 K), 1987605 (**2**–200 K), and 1987606 (**2**–260 K).†

Physical measurements

Elemental analyses. Elemental analyses (CHN) were performed with a Vario Micro Cube (Elementar) CHNOS elemental analyzer.

FT-IR spectroscopy. IR spectra were recorded at 293 K using a PerkinElmer Spectrum Two™ FT-IR equipped with an ATR sampling accessory (wavelength range: 4000–400 cm^{-1}). Spectra were recorded at 4 cm^{-1} resolution.

Optical measurements. The system for monitoring the spin crossover by changing the intensity of the reflected light consisted of an optical microscope Optica SZM-1 equipped with the camera Sigeta UCMOS 1300. The sample temperature was controlled with a Linkam optical cryostat DSC600. The cooling/heating rate was 2 K min^{-1}. Before starting the experiment, we carried out the procedure of purging air from the stage chamber with dry nitrogen. Photographs were taken automatically using ToupView software (1 image per K). Image processing was performed using ImageJ software.

Magnetic measurements. Magnetic susceptibilities were measured in the temperature range 12–360 K for **1** and **2** using a MPMS3 SQUID magnetometer (Quantum Design Inc.), in DC mode, under a DC magnetic field of 1000 Oe. Cooling and heating rates were 2 K min^{-1}. All data were corrected for the diamagnetic contributions of the sample holder and the samples estimated from Pascal's constants.[67]

Calorimetric measurements. Differential scanning calorimetry measurements were carried out using a PerkinElmer DSC 8500 operating at 50 K min^{-1} in the temperature range of 97–303 K.

X-ray powder diffraction. Powder diffractograms of the pure compounds **1** and **2** were collected at room temperature on a Shimadzu XRD-6000 diffractometer (λ = 1.54 Å) using Cu-Kα radiation over the 2θ scan range of 5°–60° and a 0.02° scan step size. PXRD patterns of **1** and **2** in high spin (HS) forms were compared to those simulated from the single crystal XRD data in the HS state. The calculated patterns were generated using Mercury software.

Raman spectroscopy. Raman spectra were recorded using a Horiba Scientific LabRam HR Evolution spectrometer in the 25–1650 cm^{-1} frequency range. A green laser with a 1% ND filter was used for Raman excitation at 532 nm. Temperature control was realized using a Linkam THMS 600 cryostat. The following parameters were used: acquisition time 100 s; 3 accumulations; grating 600 g mm^{-1}.

Conflicts of interest

There are no conflicts to declare.

Acknowledgements

This work was supported by H2020-MSCA-RISE-2016 Project 734322 and Projects 19BF037-01M and 19BF037-04 of the Ministry of Education and Science of Ukraine. V. Hiiuk thanks Lozynskyj Foundation and Yuchymenko Family Endowment Fund for financial support. The financial support of the EXCALIBUR project (Contract No. 18 PFE/16.10.2018) is also acknowledged.

Notes and references

1 A. Hauser, in *Spin-Crossover Materials. Properties and Applications*, ed. M. A. Halcrow, 2013.
2 P. Gütlich, A. B. Gaspar and Y. Garcia, *Beilstein J. Org. Chem.*, 2013, **9**, 342–391.
3 A. Bousseksou, G. Molnár, L. Salmon and W. Nicolazzi, *Chem. Soc. Rev.*, 2011, **40**, 3313–3335.
4 M. C. Muñoz and J. A. Real, *Coord. Chem. Rev.*, 2011, **255**, 2068–2093.
5 S. Brooker, *Chem. Soc. Rev.*, 2015, **44**, 2880–2892.
6 K. Senthil Kumar and M. Ruben, *Coord. Chem. Rev.*, 2017, **346**, 176–205.
7 H. J. Shepherd, I. A. Gural'skiy, C. M. Quintero, S. Tricard, L. Salmon, G. Molnár and A. Bousseksou, *Nat. Commun.*, 2013, **4**, 2607.
8 T. Miyamachi, M. Gruber, V. Davesne, M. Bowen, S. Boukari, L. Joly, F. Scheurer, G. Rogez, T. K. Yamada, P. Ohresser, E. Beaurepaire and W. Wulfhekel, *Nat. Commun.*, 2012, **3**, 938.
9 I. A. Gural'skiy, C. M. Quintero, J. S. Costa, P. Demont, G. Molnár, L. Salmon, H. J. Shepherd and A. Bousseksou, *J. Mater. Chem. C*, 2014, **2**, 2949–2955.
10 I. A. Gural'skiy, B. O. Golub, S. I. Shylin, V. Ksenofontov, H. J. Shepherd, P. R. Raithby, W. Tremel and I. O. Fritsky, *Eur. J. Inorg. Chem.*, 2016, **2016**, 3191–3195.
11 I. A. Gural'skiy, S. I. Shylin, B. O. Golub, V. Ksenofontov, I. O. Fritsky and W. Tremel, *New J. Chem.*, 2016, **40**, 9012–9016.
12 A. Djemel, O. Stefanczyk, M. Marchivie, E. Trzop, E. Collet, C. Desplanches, R. Delimi and G. Chastanet, *Chem. – Eur. J.*, 2018, **24**, 14760–14767.

13 F. J. Valverde-Muñoz, M. Seredyuk, M. C. Muñoz, K. Znovjyak, I. O. Fritsky and J. A. Real, *Inorg. Chem.*, 2016, **55**, 10654–10665.
14 O. I. Kucheriv, S. I. Shylin, V. Ksenofontov, S. Dechert, M. Haukka, I. O. Fritsky and I. A. Gural'skiy, *Inorg. Chem.*, 2016, **55**, 4906–4914.
15 L. Piñeiro-López, M. Seredyuk, M. C. Muñoz and J. A. Real, *Chem. Commun.*, 2014, **50**, 1833–1835.
16 V. Niel, J. M. Martinez-Agudo, M. C. Muñoz, A. B. Gaspar and J. A. Real, *Inorg. Chem.*, 2001, **40**, 3838–3839.
17 V. M. Hiiuk, S. Shova, A. Rotaru, V. Ksenofontov, I. O. Fritsky and I. A. Gural'skiy, *Chem. Commun.*, 2019, **55**, 3359–3362.
18 V. Niel, A. Galet, A. B. Gaspar, M. C. Muñoz and J. A. Real, *Chem. Commun.*, 2003, **3**, 1248–1249.
19 V. Niel, A. L. Thompson, M. C. Muñoz, A. Galet, A. E. Goeta and J. A. Real, *Angew. Chem., Int. Ed.*, 2003, **42**, 3760–3763.
20 V. Niel, A. L. Thompson, A. E. Goeta, C. Enachescu, A. Hauser, A. Galet, M. C. Muñoz and J. A. Real, *Chem. – Eur. J.*, 2005, **11**, 2047–2060.
21 A. Galet, M. C. Muñoz, A. B. Gaspar and J. A. Real, *Inorg. Chem.*, 2005, **44**, 8749–8755.
22 G. Agustí, A. B. Gaspar, M. C. Muñoz and J. A. Real, *Inorg. Chem.*, 2007, **46**, 9646–9654.
23 G. Agustí, A. L. Thompson, A. B. Gaspar, M. C. Muñoz, A. E. Goeta, J. A. Rodríguez-Velamazán, M. Castro, R. Burriel and J. A. Real, *Dalton Trans.*, 2008, 642–649.
24 T. Kitazawa, Y. Gomi, M. Takahashi, M. Takeda, M. Enomoto, A. Miyazaki and T. Enoki, *J. Mater. Chem.*, 1996, **6**, 119–121.
25 T. Kitazawa, M. Eguchi and M. Takeda, *Mol. Cryst. Liq. Cryst. Sci. Technol., Sect. A*, 2000, **341**, 527–532.
26 M. Seredyuk, A. B. Gaspar, V. Ksenofontov, M. Verdaguer, F. Villain and P. Gütlich, *Inorg. Chem.*, 2009, **48**, 6130–6141.
27 T. Kosone, I. Tomori, C. Kanadani, T. Saito, T. Mochida and T. Kitazawa, *Dalton Trans.*, 2010, **39**, 1719–1721.
28 T. Kosone, Y. Suzuki, S. Ono, C. Kanadani, T. Saito and T. Kitazawa, *Dalton Trans.*, 2010, **39**, 1786–1790.
29 M. Seredyuk, A. B. Gaspar, V. Ksenofontov, Y. Galyametdinov, M. Verdaguer, F. Villain and P. Gütlich, *Inorg. Chem.*, 2010, **49**, 10022–10031.
30 J. A. Rodríguez-Velamazán, C. Carbonera, M. Castro, E. Palacios, T. Kitazawa, J.-F. Létard and R. Burriel, *Chem. – Eur. J.*, 2010, **16**, 8785–8796.
31 F. L. Liu and J. Tao, *Chem. – Eur. J.*, 2017, **23**, 18252–18257.
32 F. J. Valverde-Muñoz, M. C. Muñoz, S. Ferrer, C. Bartual-Murgui and J. A. Real, *Inorg. Chem.*, 2018, **57**, 12195–12205.
33 T. Kosone, Y. Makido, S. Okuda, A. Haigo, T. Kawasaki, D. Akahoshi, T. Saito and T. Kitazawa, *Crystals*, 2019, **9**, 370.
34 V. Niel, M. C. Muñoz, A. B. Gaspar, A. Galet, G. Levchenko and J. A. Real, *Chem. – Eur. J.*, 2002, **8**, 2446–2453.
35 A. Galet, M. C. Muñoz, V. Martínez and J. A. Real, *Chem. Commun.*, 2004, **10**, 2268–2269.
36 A. Galet, M. C. Muñoz and J. A. Real, *Inorg. Chem.*, 2006, **45**, 4583–4585.
37 M. C. Muñoz, A. B. Gaspar, A. Galet and J. A. Real, *Inorg. Chem.*, 2007, **46**, 8182–8192.
38 J. A. Rodríguez-Velamazán, M. Castro, E. Palacios, R. Burriel, T. Kitazawa and T. Kawasaki, *J. Phys. Chem. B*, 2007, **111**, 1256–1261.
39 G. Agustí, M. C. Muñoz, A. B. Gaspar and J. A. Real, *Inorg. Chem.*, 2008, **47**, 2552–2561.
40 G. Agustí, S. Cobo, A. B. Gaspar, G. Molnár, N. O. Moussa, V. Pálfi, C. Vieu, M. C. Muñoz and J. A. Real, *Chem. Mater.*, 2008, **20**, 6721–6732.
41 K. Nakao, S. Hayami, M. Akita and K. Inoue, *Chem. Lett.*, 2008, **37**, 292–293.
42 L. Piñeiro-López, F. J. Valverde-Muñoz, M. Seredyuk, C. Bartual-Murgui, M. C. Muñoz and J. A. Real, *Eur. J. Inorg. Chem.*, 2018, **2018**, 289–296.
43 Y. Garcia, V. Niel, M. C. Muñoz and J. A. Real, *Topics in Current Chemistry*, 2004, vol. 233, pp. 229–257.
44 N. F. Sciortino and S. M. Neville, *Aust. J. Chem.*, 2014, **67**, 1553.
45 J. E. Clements, J. R. Price, S. M. Neville and C. J. Kepert, *Angew. Chem., Int. Ed.*, 2016, **55**, 15105–15109.
46 W. Liu, Y. Peng, S. Wu, Y. Chen, M. N. Hoque, Z. Ni, X. Chen and M.-L. Tong, *Angew. Chem., Int. Ed.*, 2017, **56**, 14982–14986.
47 C.-J. Zhang, K.-T. Lian, G.-Z. Huang, S. Bala, Z.-P. Ni and M.-L. Tong, *Chem. Commun.*, 2019, **55**, 11033–11036.
48 F.-L. Liu, D. Li, L.-J. Su and J. Tao, *Dalton Trans.*, 2018, **47**, 1407–1411.
49 S. Bonhommeau, G. Molnár, A. Galet, A. Zwick, J.-A. Real, J. J. McGarvey and A. Bousseksou, *Angew. Chem., Int. Ed.*, 2005, **44**, 4069–4073.
50 W. Liu, L. Wang, Y.-J. Su, Y.-C. Chen, J. Tucek, R. Zboril, Z.-P. Ni and M.-L. Tong, *Inorg. Chem.*, 2015, **54**, 8711–8716.
51 I. A. Gural'skiy, S. I. Shylin, V. Ksenofontov and W. Tremel, *Eur. J. Inorg. Chem.*, 2019, **2019**, 4532–4537.
52 P. Guionneau, M. Marchivie, G. Bravic, J.-F. Létard and D. Chasseau, *Top. Curr. Chem.*, 2004, **234**, 97–128.
53 S. Cobo, D. Ostrovskii, S. Bonhommeau, L. Vendier, G. Molnár, L. Salmon, K. Tanaka and A. Bousseksou, *J. Am. Chem. Soc.*, 2008, **130**, 9019–9024.
54 W. Scherer, A. C. Dunbar, J. E. Barquera-Lozada, D. Schmitz, G. Eickerling, D. Kratzert, D. Stalke, A. Lanza, P. Macchi, N. P. M. Casati, J. Ebad-Allah and C. Kuntscher, *Angew. Chem., Int. Ed.*, 2015, **54**, 2505–2509.
55 W. Scherer, *Acta Crystallogr., Sect. A: Found. Adv.*, 2016, **72**, 87.
56 M. Brookhart, M. L. H. Green and G. Parkin, *Proc. Natl. Acad. Sci. U. S. A.*, 2007, **104**, 6908–6914.
57 A. N. Gupta, V. Kumar, V. Singh, K. K. Manar, M. G. B. Drew and N. Singh, *CrystEngComm*, 2014, **16**, 9299–9307.
58 H. V. Huynh, L. R. Wong and P. S. Ng, *Organometallics*, 2008, **27**, 2231–2237.
59 Y. Meng, Q. Sheng, M. N. Hoque, Y. Chen, S. Wu, J. Tucek, R. Zboril, T. Liu, Z.-P. Ni and M.-L. Tong, *Chem. – Eur. J.*, 2017, **23**, 10034–10037.

60 T. Kosone, T. Kawasaki, I. Tomori, J. Okabayashi and T. Kitazawa, *Inorganics*, 2017, **5**, 55.
61 P. Gütlich and H. A. Goodwin, *Spin Crossover in Transition Metal Compounds I*, 2004, pp. 13–14.
62 G. Molnár, V. Niel, A. B. Gaspar, J.-A. Real, A. Zwick, A. Bousseksou and J. J. McGarvey, *J. Phys. Chem. B*, 2002, **106**, 9701–9707.
63 J. A. Wolny, R. Diller and V. Schünemann, *Eur. J. Inorg. Chem.*, 2012, **2012**, 2635–2648.
64 G. M. Sheldrick, *Acta Crystallogr., Sect. C: Struct. Chem.*, 2015, **71**, 3–8.
65 G. M. Sheldrick, *Acta Crystallogr., Sect. A: Found. Crystallogr.*, 2008, **64**, 112–122.
66 O. V. Dolomanov, L. J. Bourhis, R. J. Gildea, J. A. K. Howard and H. Puschmann, *J. Appl. Crystallogr.*, 2009, **42**, 339–341.
67 G. A. Bain and J. F. Berry, *J. Chem. Educ.*, 2008, **85**, 532.